Applied Surface Science

First-Principles Study on the stability, electronic structure, and band alignment of AgNbO3 surfaces: understanding the adsorption process of H2O and O2

Manuscript Number:	APSUSC-D-24-08688
Article Type:	Full Length Article
Keywords:	AgNbO3; DFT calculations; surfaces; adsorption of H2O and O2; reactive oxygen species
Corresponding Author:	Marisa Carvalho de Oliveira Federal University of Sao Carlos São Carlos, São Paulo BRAZIL
First Author:	Marisa Carvalho de Oliveira
Order of Authors:	Marisa Carvalho de Oliveira
	Elson Longo
	Renan A. P. Ribeiro
	Samantha C. S. Lemos
	Juan Andrés
	Lourdes Gracia
Abstract:	In this work, DFT calculations have been employed to delve into the structural, electronic, and optical properties of low-index (010), (100), (101), (110), (011), and (114) surfaces of AgNbO3. Wulff construction was used to predict the available morphologies of this material and their transformations, which were matched with the experimental images obtained by electron microscopy to support our findings. Our data indicate that the undercoordinated O anions and Ag and Nb cations on these surfaces act as frustrated Lewis base and acid pairs, respectively, to control their structure and electronic properties. These sites at the (110) and (010) selectively bind H2O and O2 molecules, opening an energetically favorable pathway for the dissociation of H2O to enhance the initial stages of the formation of reactive oxygen species, ·OH, ·O2- and ·OOH radicals, which adsorbed strongly on both surfaces within a simplified model. Overall, the results demonstrate that careful consideration of the impacts of surface chemistry on the behavior of AgNbO3 surfaces is required to further understand and tailor the reactivity based on the generation of these highly reactive species.

First-Principles Study on the stability, electronic structure, and band alignment of $AgNbO_3$ surfaces: understanding the adsorption process of H_2O and O_2

Marisa Carvalho de Oliveira[1,2*], Elson Longo[2], Renan A. P. Ribeiro[3], Samantha C. S. Lemos[4], Juan Andrés[4*] and Lourdes Gracia[1*]

[1]Department of Physical Chemistry, University of Valencia, 46010 Valencia, Spain.

[2]Functional Materials Development Center (CDMF), Federal University of São Carlos – UFSCar, 13565-905, São Carlos – SP, Brazil.

[3]Department of Natural Science, Minas Gerais State University – UEMG, Av. Paraná, 3001, CEP 35501-170, Divinópolis – MG, Brazil

[4]Department of Physical and Analytical Chemistry, University Jaume I – UJI, 12071 Castellon, Spain.

Corresponding authors: marisacoliveira31@gmail.com, lourdes.gracia@uv.es, andres@qfa.uji.es

Abstract

In this work, DFT calculations have been employed to delve into the structural, electronic, and optical properties of low-index (010), (100), (101), (110), (011), and (114) surfaces of $AgNbO_3$. Wulff construction was used to predict the available morphologies of this material and their transformations, which were matched with the experimental images obtained by electron microscopy to support our findings. Our data indicate that the undercoordinated O anions and Ag and Nb cations on these surfaces act as frustrated Lewis base and acid pairs, respectively, to control their structure and electronic properties. These sites at the (110) and (010) selectively bind H_2O and O_2 molecules, opening an energetically favorable pathway for the dissociation of H_2O to enhance the initial stages of the formation of reactive oxygen species, ·OH, $\cdot O_2^-$ and ·OOH radicals, which adsorbed strongly on both surfaces within a simplified model. Overall, the results demonstrate that careful consideration of the impacts of surface chemistry on the behavior of $AgNbO_3$ surfaces is required to further understand and tailor the reactivity based on the generation of these highly reactive species.

Keywords: $AgNbO_3$, DFT calculations, surfaces, adsorption of H_2O and O_2, reactive oxygen species.

1. Introduction

The remarkable properties of semiconductors based on transition metal oxides, such as electrical, optical, thermal, and antimicrobial, largely depend on structure, exposed surfaces at the morphology, and other tunable characteristics that form the backbone of many industrial processes, including catalysis, photocatalysis, sensing, among others.[1-4] The arrangement of atoms is generally different for each surface, which can lead to differences in electronic properties that often can define the surface chemistry as well as the reactivity.[5, 6]

In the field of photocatalyst, the surface atomic arrangement and the related electronic configuration provide the active sites for the photogenerated charge carrier transfer, which can be fine-tuned.[7, 8] Specifically, the generated electron-hole pairs at the surfaces may react with H_2O and O_2 to form reactive oxygen species (ROS), such as hydroxyl radical (·OH) and superoxide radical ($\cdot O_2$), respectively. The effectiveness of these transformations not only depends on the surface atomic arrangements of these complex oxides but also on the alignment of the conduction band (CB) and valence band (VB) of the exposed surfaces and the redox potential of the target reactions involving both H_2O and O_2 molecules, increasing the probability of ROS generation.[9, 10] This alignment would favor the transfer of photoexcited electrons from CB to O_2 to form $\cdot O_2$, while the photoexcited holes at the VB can react with H_2O to generate ·OH along a splitting process

ROS are the basis of advanced oxidation processes, such as oxidative stress, which is the condition where there is an imbalance between the generation and elimination of ROS, which, in turn, has a strong impact, during their short lifetime, on cells and tissues of organisms to cause serious damage to nucleic acids, lipids, and proteins, and inhibit or exterminate microorganisms and pathogens and it is frequently observed in several diseases.[11-13], and triggers antimicrobial effects by oxidizing membrane lipids and other essential bacterial components on the semiconductor's surface.[14, 15] In addition they can decompose organic and inorganic compounds to transform contaminants into less damaging materials, organic synthesis, or heterogeneous catalysis.[16-21] Therefore, controlling the surface structure and morphology and modulation of electronic properties of transition metal oxides has been an emerging theme to reveal the role that redox chemistry plays in optimizing their functionalities.

Silver niobate ($AgNbO_3$) is a complex metal oxide that contains two d transition metals, Ag and Nb, with a small band gap (~2.8 eV), and it has recently been attracting a lot of interest for its excellent properties, which can find applications in many fields[22]

due to its high electrical conductivity[23, 24], photoluminescence emissions[25, 26] and it has shown good antimicrobial capabilities and very low toxicity.[27-29] $AgNbO_3$ exhibits ferroelectric properties, which can effectively promote the migration of photo-generated carriers responsible for the piezo-photocatalytic process to lead to efficient redox reactions on the catalyst surface for the degradation of different pollutants,[30-34] which are mainly attributed to the generation of $\cdot O_2^-$ and ·OH radicals from low-reactivity O_2 and H_2O, respectively.[35] The presence of these ROS is regulated by the exposed crystal surfaces in their morphology, defining how they interact with their environment and how they are absorbed, formed, and react with molecules and cells and, by extension, their effectiveness in application possibilities.[34] This control over exposed surfaces at the morphology with specific atomistic structures allows us to tailor these materials with desired properties for specific purposes and develop morphology–property relationships, enhancing their performance to open new guides of their rational design. However, atomic-scale details of surfaces and their geometry and electronic properties are difficult or impossible to ascertain experimentally.

At this point, we must stress that most of the theoretical works have focused on the bulk, and less attention has been paid to surface-related properties of $AgNbO_3$,. Therefore, investigations on the surface structure, associated acid-base chemistry, and how the resulting surface changes by the adsorption process of H_2O and O_2 to induce the generation of ROS precursors at the surface are needed to improve their performance for many applications further. In a joint experimental and theoretical study, our research group recently disclosed the surface reactions of H_2O and O_2 on the Ag_3PO_4 (110) surface for the initial stages of ROS production.[36] In this systematic study, we perform DFT calculations to determine the bulk structure, stability, electronic structure, and band alignment of different terminated low-index (010), (100), (101), (110), (011), and (114) surfaces of $AgNbO_3$. Within the framework of a simplified model, we analyze the adsorption of H_2O and O_2 molecules, as well the dissociation of H_2O on (110) and (010) surfaces to disclose the initial steps for the formation of the precursors of ·OH, $\cdot O_2^-$, and ·OOH radicals at these surfaces**.** This research is expected to help identify optimally exposed surfaces at the morphology, opening perspectives to drastically improve their performance as photocatalysts and biocidal material.

The paper is organized as follows. First, we will briefly overview computational methods and model systems. Subsequently, we will present and discuss the results. First, the geometry, stability, and electronic properties of the bulk and different surfaces, using

the density of states (DOS) and Bader charge analysis. Next, we will present and discuss the results on the individual and co-adsorption processes of H_2O and O_2 molecules on (110), (114), and (010) surfaces. Then, the dissociation process of H_2O at the (010) surface is investigated to gain insight into the nature of the initial steps for the formation of the precursors of ·OH, $\cdot O_2^-$, and ·OOH radicals at these surfaces. Finally, the conclusion section closes this article.

2. Computational Methods and Model Systems

In this study, the structural and electronic properties of $AgNbO_3$ bulk and surface models were studied by first-principles calculations at the DFT/WC1LYP[37] level as implemented in CRYSTAL17.[38] Such hybrid functional was selected due to the validation of previous studies for ferroelectric materials like $LiNbO_3$ and $LiTaO_3$.[39] The Ag and Nb centers were described by the effective core pseudopotential HAYWSC-311d31G[40, 41], while O and H centers were described by an all-electron GTO basis set defined as 8-411G(d) and 3-11G(p).[41, 42] The evaluation of the Coulomb and exchange series was truncated to 10^{-7} for the Coulomb overlap tolerance, 10^{-7} for the Coulomb penetration tolerance, 10^{-7} for the exchange overlap tolerance, 10^{-7} for the exchange pseudo-overlap in the direct space, and 10^{-14} for the exchange pseudo-overlap in the reciprocal space. The condition for the SCF convergence was set to 10^{-7} a.u. for the total energy difference between two subsequent cycles. Furthermore, default thresholds for geometry optimization within the CRYSTAL code were used for all atoms: while the maximum and root-mean-square (rms) forces were set to 0.000450 and 0.000300 a.u., the maximum and rms atomic displacements were set to 0.001800 and 0.001200 a.u., respectively. The k-space sampling for the geometry optimization included a 6 × 6 × 6 (bulk) and 4 x 4 x 1 (surface) Monkhorst−Pack mesh. The orthorhombic structure (*Pbcm*) was considered for the bulk model, and the (010), (100), (101), (110), (011) low index, and (114) surfaces were selected as non-polar, symmetric, and stoichiometric models. The (111) low-index and high-index (112) surfaces were not considered due to the polar behavior and their convergence problems as functions of the slab thickness. In addition, the (114) surface with a low value of surface energy (E_{surf}), as recently reported, has also been studied.[43]

The equilibrium morphologies of nanoparticles can be obtained once the specific E_{surf} of exposed crystallographic surfaces is calculated. In the present case, the E_{surf} values were obtained using the following equation:

$$\mathbf{E_{surf}} = \frac{(\mathbf{E_{slab}} - \mathbf{nE_{bulk}})}{\mathbf{2A}} \quad (\mathbf{1})$$

where E_{slab} and E_{bulk} correspond to the total energy of slab and bulk models, respectively, n is the number of bulk units in the slab and A is the surface area for symmetric slabs. The E_{surf} values were optimized as a function of the slab thickness, being all models represented by 16 unit formulas and thickness of 10.60 Å (010), 10.52 Å (100), 11.19 Å (101), 8.41 Å (110), 12.04 Å (011) and 6.33 Å (114), respectively. Using the calculated E_{surf} values and the Wulff construction, we can obtain the ideal and available morphologies of $AgNbO_3$ and their possible transformations by tuning the E_{surf} of the different surfaces.[44-47] Further, the calculated and matched with the experimental electron microscopy images reported in the literature can be compared.

The O_2 and H_2O adsorption energies $\boldsymbol{E_{ads}}$ on the surfaces of $AgNbO_3$ were computed following the equation:

$$\boldsymbol{E_{ads}} = [\boldsymbol{E_{(slab+O_2/H_2O)}} - (\boldsymbol{E_{slab}} + \boldsymbol{E_{O_2/H_2O}}) + \boldsymbol{E_{BSSE}}] \quad (\mathbf{2})$$

where $\boldsymbol{E_{(slab+O_2/H_2O)}}$ is the total energy of the optimized slab with adsorbed O_2/H_2O molecules, $\boldsymbol{E_{slab}}$ is the total energy of the isolated optimized slab, and $\boldsymbol{E_{O_2/H_2O}}$ is the total energy of O_2 and H_2O molecules in the gas phase. The basis set superposition error (BSSE) was calculated following the expression:

$$\boldsymbol{E_{BSSE}} = \left(\boldsymbol{E_{slab}^{frozen}} - \boldsymbol{E_{slab+ghost}^{frozen}}\right) + \left(\boldsymbol{E_{O_2/H_2O}^{frozen}} - \boldsymbol{E_{O_2/H_2O+ghost}^{frozen}}\right) \quad (\mathbf{3})$$

where all the energies refer to the geometries of the two separated moieties (slab + O_2/H_2O) frozen in the minimum adsorption configuration, with and without ghost functions, respectively. All minima were confirmed by obtaining only positive frequencies.

The H_2O dissociation energy $\boldsymbol{E_{diss}}$ on the surfaces of $AgNbO_3$ was computed following the equation:

$$\boldsymbol{E_{diss}} = [\boldsymbol{E_{(slab+OH+H)}} - (\boldsymbol{E_{slab}} + \boldsymbol{E_{H_2O}}) + \boldsymbol{E_{BSSE}}] \quad (\mathbf{4})$$

The density of states, DOS (total and projected on atoms and orbitals) and band structure profiles were calculated based on the optimized wavefunction of $AgNbO_3$ bulk and their (010), (100), (101), (110), (011), and (114) surfaces to understand the degree of contribution of the different orbitals of the atoms and the interatomic bonding between both O_2 and H_2O molecules and $AgNbO_3$ surfaces.

The electron density (ρ) on atoms was computed at a regular 3D grid of points set as 80 for the adsorbate/slab system isolated slabs, and O_2 and H_2O molecules. Further, the Bader charges in the Quantum Theory of Atoms in Molecules (QTAIM) framework were computed from the electron density grid using the code developed by Henkelman et al.[48-51] The charge density difference (CDD), as a measure of the electron transfer between $AgNbO_3$ and quimiabsorbed O_2 and H_2O molecules, was calculated by using the following equation:

$$\mathbf{CDD} = \boldsymbol{\rho}_{adsorbate/slab} - \boldsymbol{\rho}_{slab} - \boldsymbol{\rho}_{molecule} \qquad (5)$$

3. Results and Discussion

3.1. Bulk structure and electronic properties

The crystal structure of $AgNbO_3$ was indexed to an orthorhombic structure with *Pbcm* space group (JCPDS 01-070-4738),[52] and it contains 8 formula units per unit cell. The bulk structure is composed of distorted eight coordination [AgO_8] and [NbO_6] octahedra clusters, which are arranged in chains composed of pairs of edge-sharing [NbO_6]. It is also observed that these chains are joined in zigzag by corner sharing between [NbO_6] in adjacent lines, confirming the non-centrosymmetric nature of $AgNbO_3$. The [AgO_8] clusters present Ag-O bond lengths of 2.497 (2x), 2.558 (1x), 2.597 (1x), 2.723 (2x), and 2.743 Å (2x), while the [NbO_6] centers display Nb-O bond distances of 1.889 (1x), 1.895 (1x), 2.007 (2x), 2.195 (1x) and 2.225 Å (1x), consistent with the distortion of the orthorhombic structure that generates ferroelectric properties.

The calculated lattice parameters for the orthorhombic structure were a = 5.665, b = 5.714, and c = 15.693 Å. These values agree with previously reported theoretical and experimental data, as summarized in **Table 1**.[53-55]

Table 1. Theoretical and experimental values for lattice parameters of $AgNbO_3$.

	a	b	c	V
This Work	5.665	5.714	15.693	507.98
Theo.[54]	5.453	5.540	15.420	465.83
Exp.[53]	5.547	5.604	15.642	486.24
Exp.[55]	5.547	5.603	15.637	485.90

The calculated DOS and band structure are shown in **Figure 1**. The valence band (VB) was mainly composed of O (2p) and Ag (4d) orbitals, while the conduction band (CB) is associated with the empty 4d orbitals of Nb. The distinct overlap of O 2p and Ag 4d orbitals in the VB is an advantage for the mobility of photogenerated charge carriers, resulting in improved photocatalytic activity. Therefore, the electronic excitation associated with the band-gap energy can be described as intermetallic charge transfer involving the Ag 4d orbitals of [AgO_8] clusters and the Nb 4d orbitals of [NbO_6] clusters mediated by O 2p orbital, i.e., one electron of the [AgO_8] cluster is excited to occupy the empty electronic level associated to [NbO_6] cluster using the O 2p orbital as bridging electronic state. The band-gap value was estimated as 2.99 eV being an indirect transition between Γ and S points, in agreement with the experimental values reported in the literature (2.78 eV).[52]

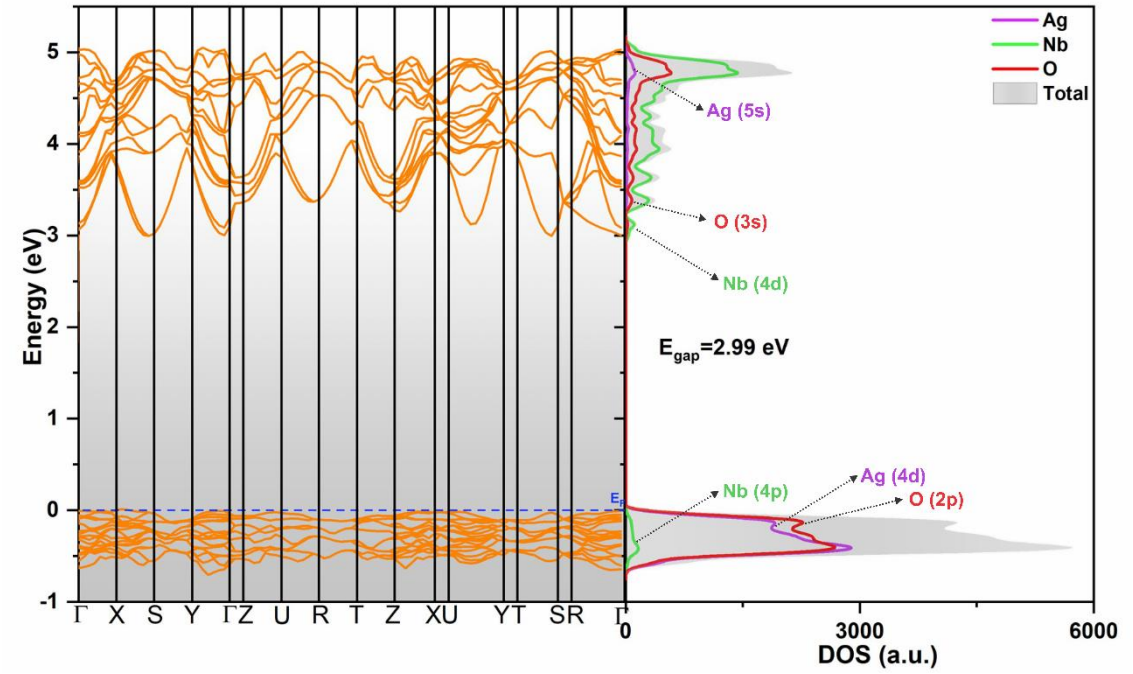

Figure 1. Band Structure and orbital-resolved DOS projections for $AgNbO_3$. In all cases, the Fermi level was set at zero.

3.2. Stability and map of morpholgies, and electronic properties of (010), (100), (101), (110), (011), and (114) surfaces

The (010), (100), (101), (110), (011) low index, and (114) surfaces, as well as the bulk structure, are depicted in **Figure 2**. The Kröger−Vink notation[56] was used to classify the number of Ag-O and W-O breaking bonds of the incomplete superficial clusters. Each surface presents coordinated and undercoordinated Ag and Nb clusters and neutral oxygen vacancies (represented by V_O).

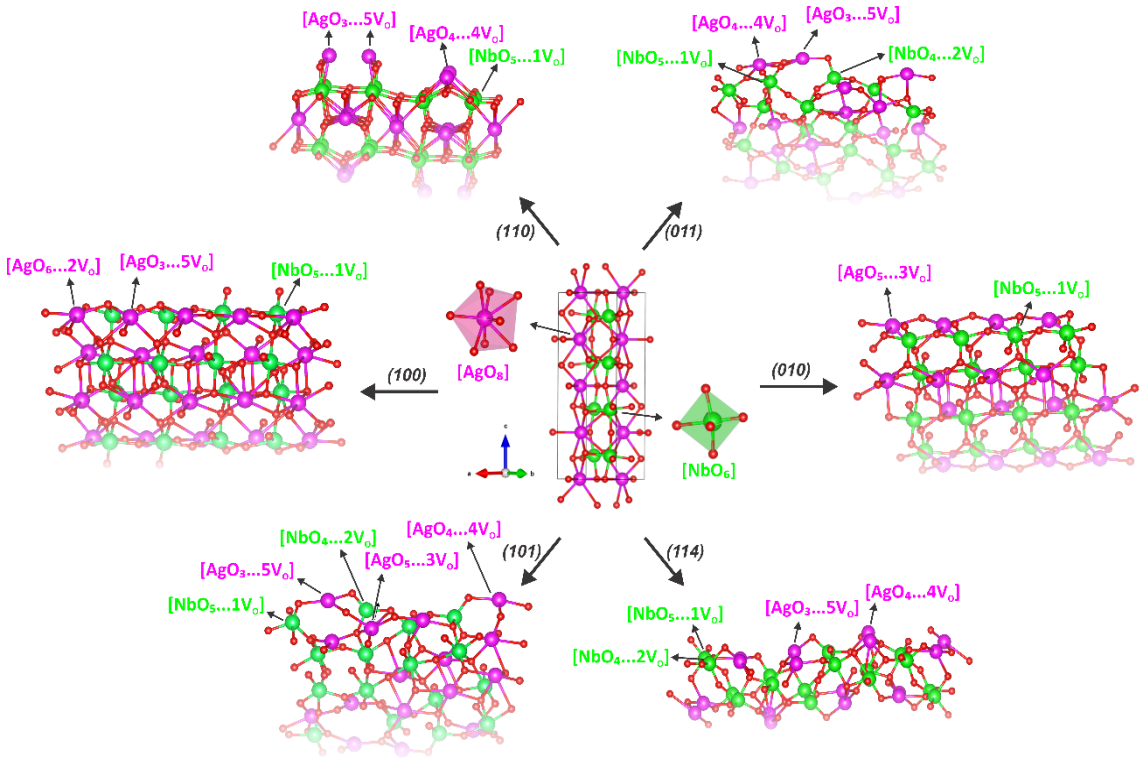

Figure 2. Schematic representation of bulk and (010), (100), (101), (110), (011), and (114) surface models of $AgNbO_3$. For clarity purposes, the type and quantity of underocoodinated clusters at each surface are depiected by using the Kröger−Vink notation.

The values of surface energy (E_{surf}) in J/m^2 follows this order: (114) < (100) < (010) < (101) < (011) < (110), as can be seen in Table 2. The (101), (011), and (110) are the most unstable surfaces, which contain a large amount of undercoordinated Ag and Nb sites. The most stable surface (114) contains four- and three-fold silver cations combined with six-, five- and four-fold Nb sites. The (010) and (100) have close values of E_{surf} with similar number and type of incomplete clusters.

Table 2. Cluster coordination of both Ag and Nb centers at the surfaces. Surface energy (E_{surf}), band-gap (E_{gap}) values are also shown.

Surface	**Cluster coordination**		**E_{surf} (J/m²)**	**E_{gap} (eV)**
	Ag	*Nb*		
(010)	$[AgO_{5...}3V_O]$	$[NbO_{5...}1V_O]$	0.65	3.33
(100)	$[AgO_6…2V_O]$ $[AgO_5…3V_O]$	$[NbO_{5...}1V_O]$	0.64	3.40
(101)	$[AgO_6…2V_O]$ $[AgO_5…3V_O]$ $[AgO_4…4V_O]$ $[AgO_3…5V_O]$	$[NbO_6]$ $[NbO_{5...}1V_O]$ $[NbO_4…2V_O]$	0.76	3.11
(110)	$[AgO_4…4V_O]$ $[AgO_3…5V_O]$	$[NbO_6]$ $[NbO_{5...}1V_O]$	0.83	2.77
(114)	$[AgO_4…4V_O]$ $[AgO_3…5V_O]$	$[NbO_6]$ $[NbO_{5...}1V_O]$ $[NbO_4…2V_O]$	0.56	3.63
(011)	$[AgO_4…4V_O]$ $[AgO_3…5V_O]$	$[NbO_6]$ $[NbO_{5...}1V_O]$ $[NbO_4…2V_O]$	0.86	2.89

By applying our methodology[46, 57, 58] and combining the calculated values of E_{surf} and the Wulff construction, we obtained the map of the available morphologies of $AgNbO_3$, as illustrated in Figure 3. The equilibrium morphology of $AgNbO_3$ obtained by the calculated values of E_{surf} of each surface displays a truncated octahedron shape that predominantly exposed the (010), (100), and (114) surfaces, accounting for 11.2%, 11,4%, and 77.4%, respectively.

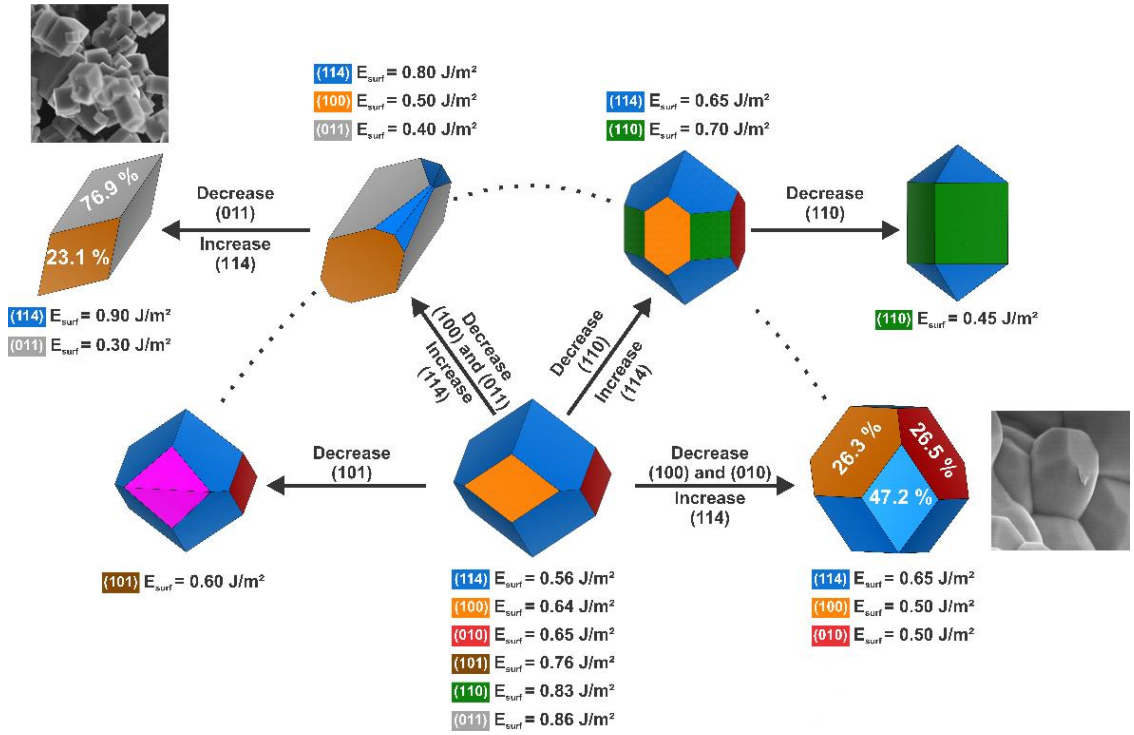

Figure 3. Map of available morphologies of $AgNbO_3$ crystals. Experimental micrographs are also included for comparison purposes. Reproduced from Ref. [59] with permission from Elsevier. Reprinted with permission from Ref. [24], Copyright 2015 American Chemical Society.

Comparing the obtained theoretical morphologies with the FE-SEM and SEM images reported in the literature [24, 59], the dodecahedron morphology (at the right part of Figure 3) was generated from the ideal morphology by decreasing the value of (100) and (010) surfaces energies to 0.50 J/m^2, and simultaneously increasing the corresponding value for (114) to 0.65 J/m^2. This morphology is composed of 47.2% of (114), 26.5% (010), and 26.3% (100). On the other hand, The prismatic morphology (at the left part of Figure 3) appears by decreasing the surface energy values of (011) to 0.30 J/m^2 and of (100) to 0.50 J/m^2, as well as increasing the (114) E_{surf} value from 0.80 to 0.90 J/m^2. This morphology comprised 76.9% of (011), and 23.1% (100).

The electronic structure of the surfaces was analyzed based on the atom-resolved DOS depicted in **Figure 4**. The band-gap values follow this order: (110) < (011) < (101) < (010) < (100) < (114), as observed in Table 2. Compared with the band-gap values for $AgNbO_3$ bulk (2.99 eV), only the (110) surface exhibited a reduced band-gap value, whereas the other surfaces presented higher band-gap values. As regards the VB and CB compositions, all calculated DOS exhibited a very similar pattern in comparison to the

bulk (Fig. 2), where the VB is composed of mixed Ag (4d) and O (2p) states and the CB is formed by empty Nb (4d) and O (3s) states, confirming that the electronic transition occurs from [AgO_n] to [NbO_n] cluster as a charge-transfer transition mechanism.

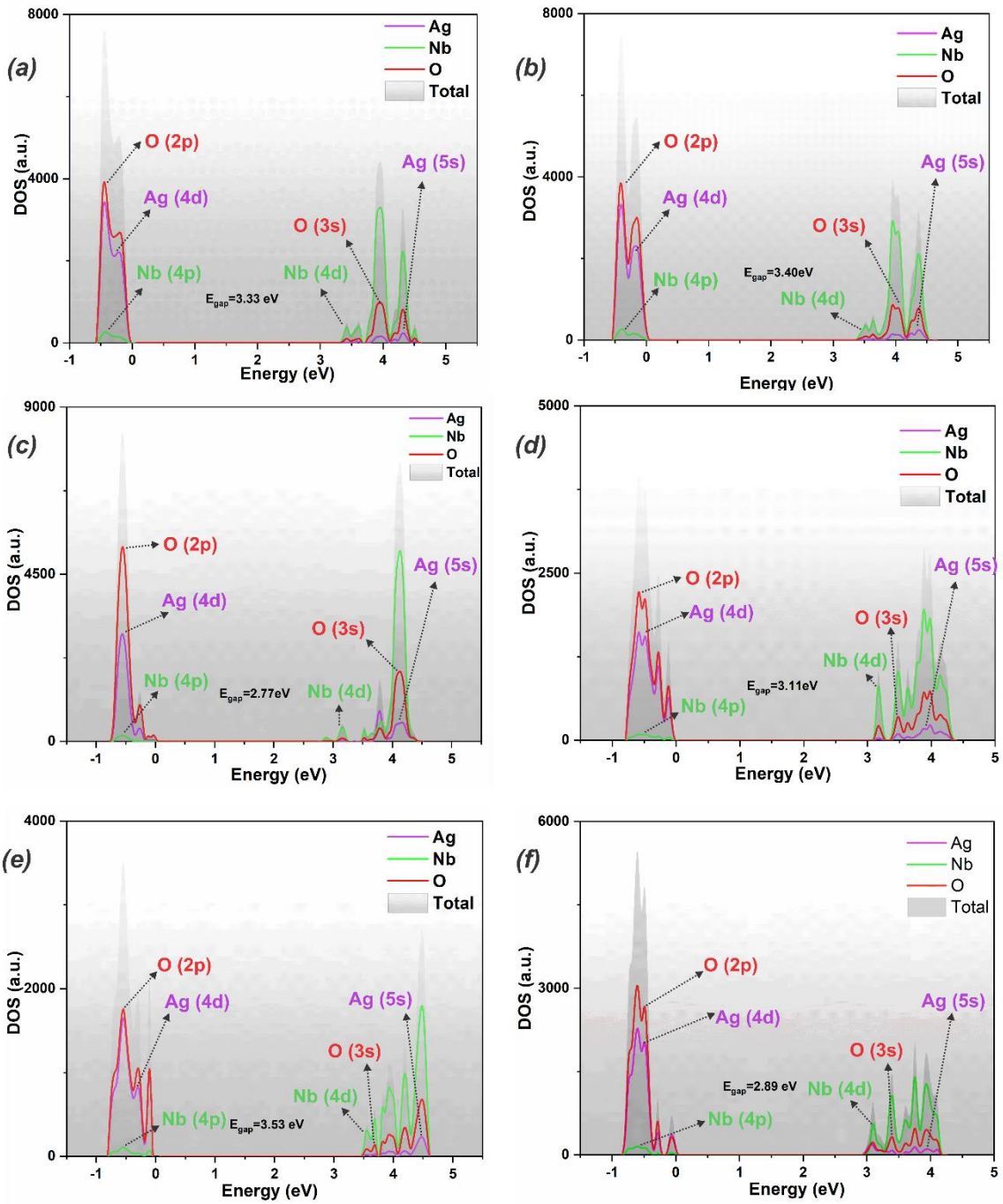

Figure 4. Orbital-resolved DOS projections for a) (010), b) (100), c) (110), d) (101), e) (114), and f) (011) surfaces of $AgNbO_3$. In all cases, the Fermi level was set at zero.

It is crucial to ensure that the positions of the VB and CB edges are more positive than the oxidation potential and more negative than the reduction potential of the redox

potentials of the desired products, or else, the reactions may not occur.[60, 61] This is because the reducing and oxidizing powers of electrons and holes, respectively, depend on the potential of these band edges and determine if the transfer of charge carriers is possible between the photocatalyst/substrate interfaces.[62] Therefore, we can predict which reactions can occur on the surface by comparing the surface band positions and the potential formation of different ROS. [46, 63] To ensure the utilization of photogenerated electrons for conversion of dissolved O_2 molecules to $^{\bullet}O_2^-$ free radicals, the conduction band should be located at a more negative potential than the -0.33 V ($O_2/{\bullet}O_2^-$), whereas for the valence band, a more positive potential than +1.90 V (•OH/OH^-) or +2.32 V (H_2O/•OH) is required, as shown in Figure 5. In addition, the potential of methane conversion from carbon dioxide is included.

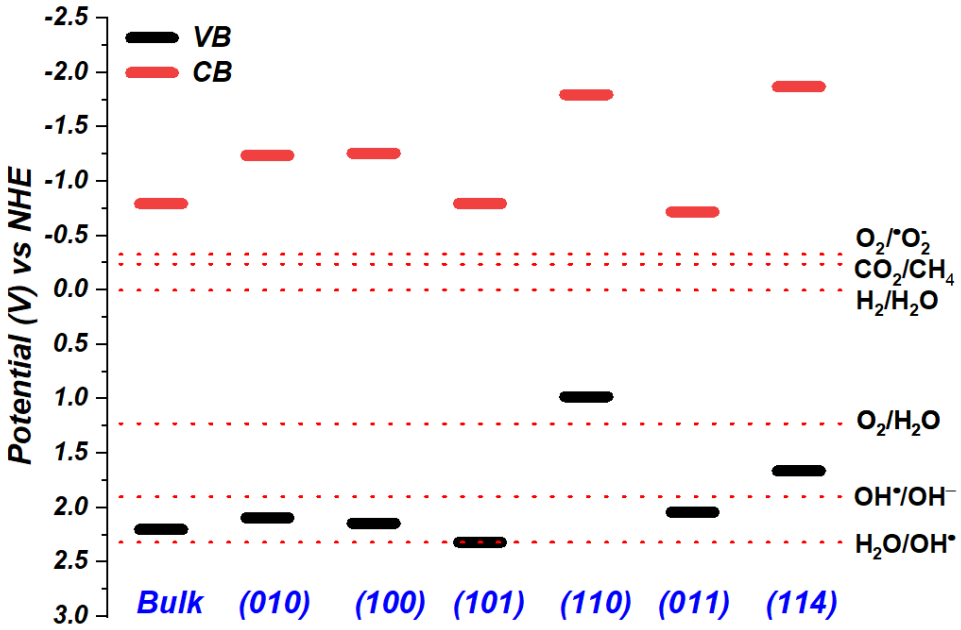

Figure 5. Calculated values of the VB and CB edge potentials for the bulk and (010), (100), (101), (110), (011), and (114), surface models of $AgNbO_3$.

In this case, it was observed that the CB potentials were calculated to be more negative than $O_2/{\bullet}O_2^-$ standard potential, indicating that excited electrons can be used to activate the adsorbed O_2 molecules to generate $\bullet O_2^-$. On the other hand, bulk, (010), (100), and (101) surface models exhibit VB edge closer to the H_2O/•OH (2.33 V vs NHE at pH = 7) standard potential, making them more reactive in comparison to (110) and (114) surfaces. An analysis of **Figure 5** renders that bulk and (010), (100), (101), (011), and

(114) surfaces are active in oxygen and hydrogen evolution reactions (OER and HER) associated with the water splitting mechanism.[64, 65]

Surface frustrated Lewis pairs (SFLPs) on metal oxides consist of proximal Lewis acid and Lewis base sites that are spatially prevented from bonding and working synergistically to induce polarization of small molecules adsorbed in the surface, allowing it to undergo heterolytic cleavage.[66] The SFLP sites on the $AgNbO_3$ surfaces include coordinate-unsaturated Lewis acid Ag or Nb atoms and an adjacent Lewis base superficial O atoms (twofold coordinated), which can serve as sites for the synergistic activation of H_2O and O_2, as depicted in **Figure 6**. Specifically, **t**he bonding and antibonding orbitals of the H_2O molecule interact simultaneously with the empty orbital of Lewis acid and the non-bonding orbital of the Lewis base, respectively. The transfer of electrons from the bonding orbitals of the H_2O molecule to the empty orbitals of the Lewis acid, as well as the transfer of lone-pair electrons from the Lewis base to the antibonding orbitals of the H_2O molecule, resulting in the polarized heteroclinic cleavage of the H_2O molecule. Then, the O_2 and H_2O adsorption processes on the $AgNbO_3$ (010), (100), (101), (011), and (114) surfaces as a first step for the generation of ROS are studied.

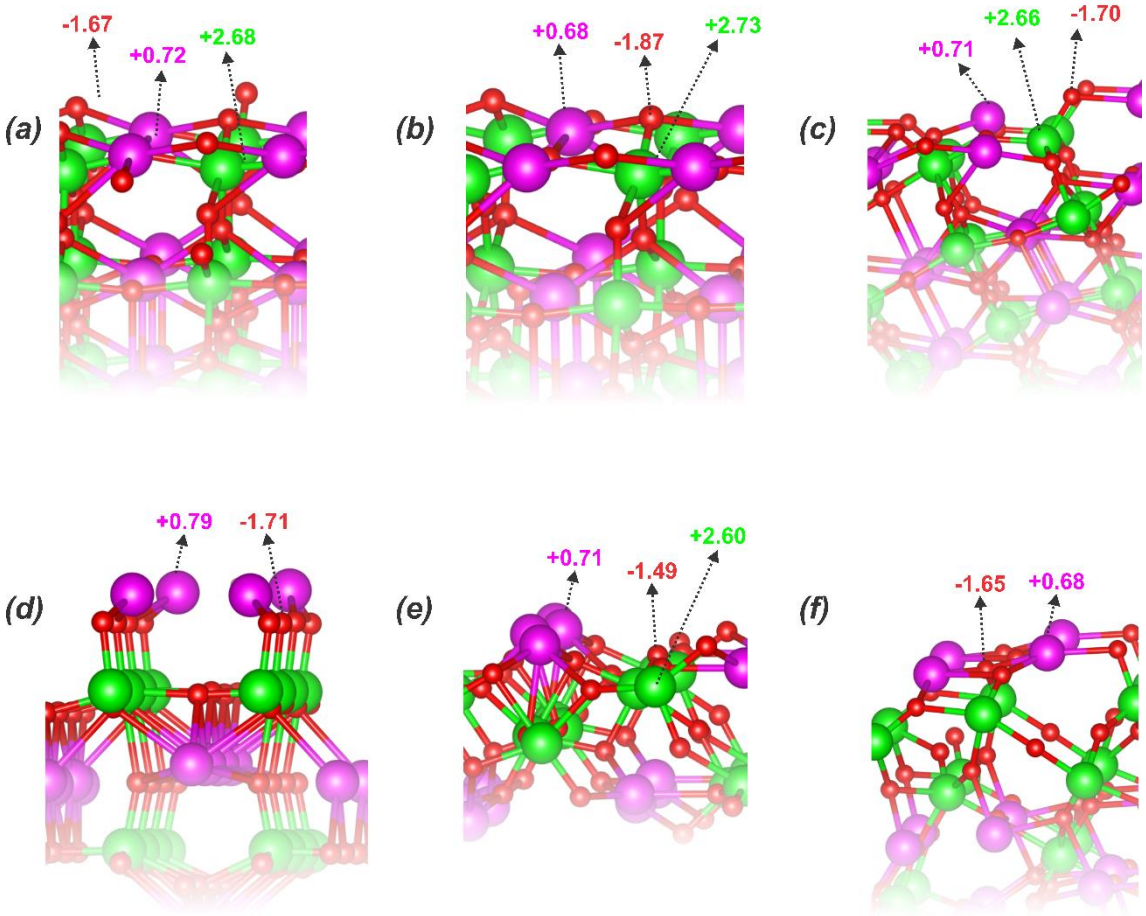

Figure 6. Bader charge values for Surface frustrated Lewis pairs of a) (010), b) (100), c) (101), d) (110), e) (114), and f) (011) surface of $AgNbO_3$.

3.3. Adsorption process of H_2O and O_2 at the surfaces

The values of E_{ads} of H_2O follow the order: (110) > (010) > (101) > (100) > (114) > (011), as can be seen in **Figure 7**. The interaction of the adsorbed H_2O molecule at the (010) and (100) surfaces occurs using the superficial Nb centers, whereas on the other surfaces, the interaction is through Ag centers. In all cases, the adsorption mechanism can be classified as a physisorption behavior with non-bonding interactions between undercoordinated Nb/Ag centers with the oxygen atom of H_2O and concomitant formation of a H-bond with adjacent oxygen anions at the surface.

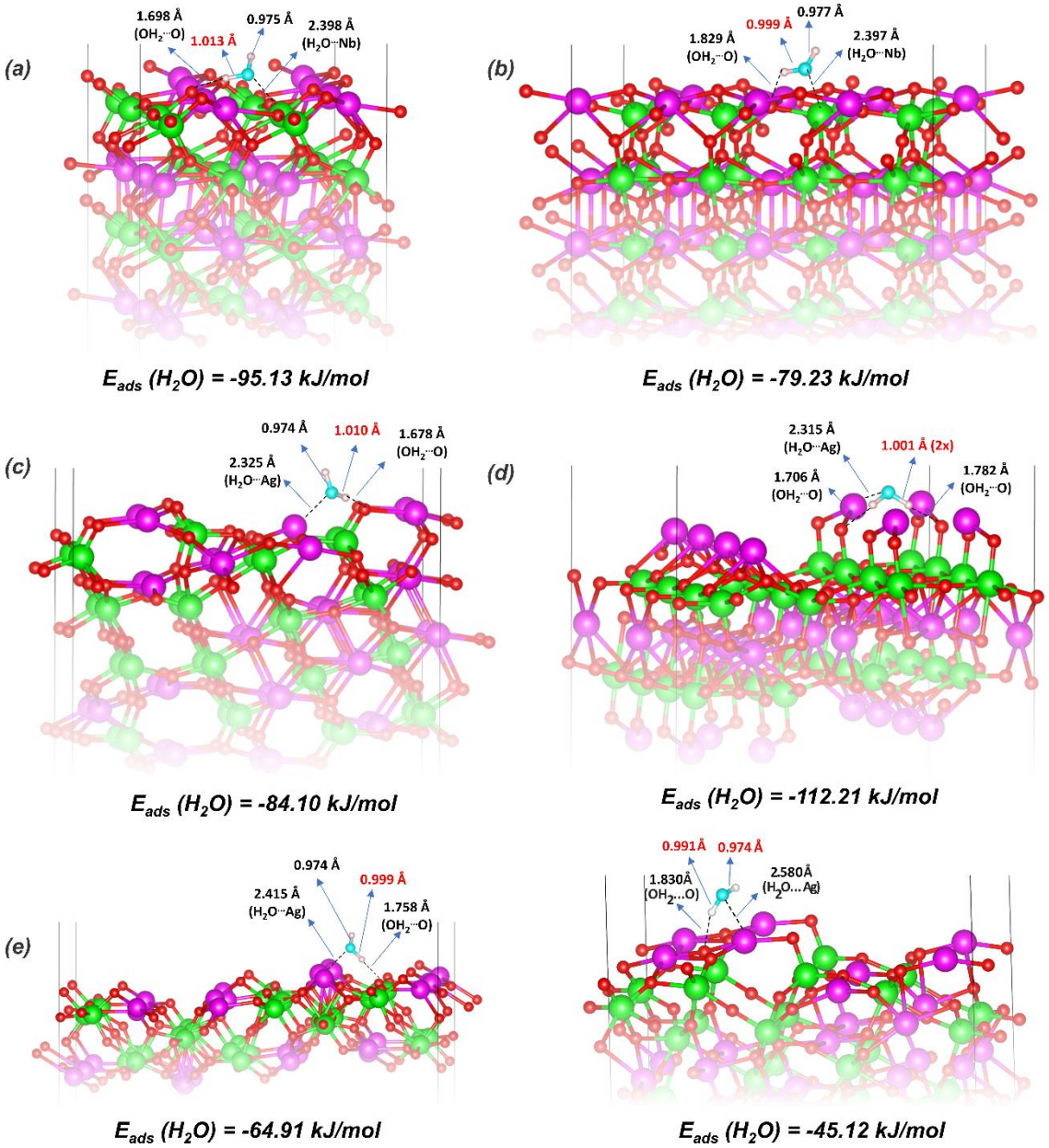

Figure 7. Side views of H_2O adsorption (cyan) on low-index surfaces a) (010), b) (100), c) (101), d) (110), e) (114), and f) (011) surface of $AgNbO_3$. Selected values of Nb-O, Ag-O, and H-O distances (Å). Values of the adsorption energies (E_{ads}) were included for comparison purposes.

Based on the optimized geometries depicted in **Figure 7**, it was observed that in all cases, one of the O-H bonds (red-color) from H_2O molecule becomes larger, suggesting that superficial undercoordinated oxygen atoms interact with H species, while OH moiety remains adsorbed on the undercoordinated Ag/Nb centers.

The water adsorption process implies an electron density transferring from H_2O to the surface, confirmed in the charge transfer isosurfaces shown in **Figure 8**.

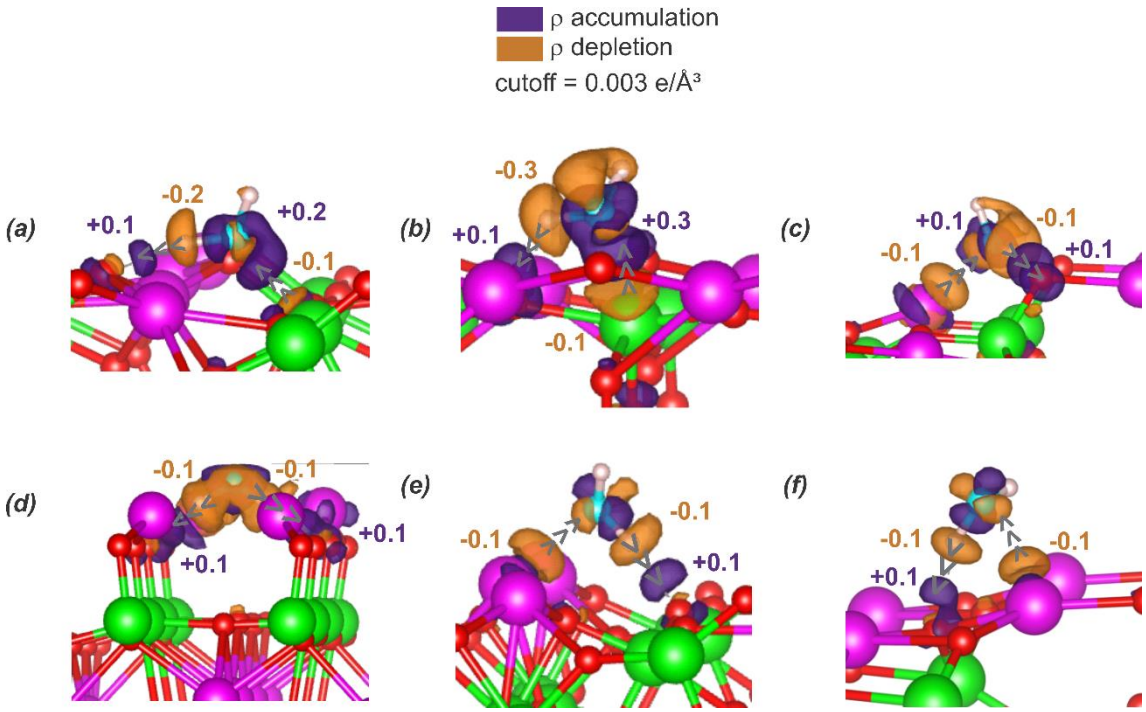

Figure 8. Charge-transfer isosurfaces (0.003 e/Å³) for H_2O (in cyan) adsorption process on a) (010), b) (100), c) (101), d) (110), e) (114) and f) (011) $AgNbO_3$ surface models.

From an inspection of **Figures 7** and **8**, it was noted that the highest adsorption energy for (110) surface (**Figure 7d**) is followed by a charge-transfer mechanism between superficial oxygen atoms that acts as acceptor (+0.1e in **Figure 8d**) from the electron density associated with the O-H water chemical bonds (-0.1e in **Figure 8d**). The higher adsorption energy was attributed to the double interaction between the O-H and superficial oxygen atoms. For the (010) and (100) surfaces (**Figures 8a and 8c**), higher amounts of electron density were transferred, involving not only the H atoms but also the oxygen that interacts with the superficial Nb cations receiving +0.2 - +0.3e from the undercoordinated cations. In other cases, the surfaces exhibited a slightly reduced charge transfer, where the major values were associated with the acceptor (+0.1e) behavior of superficial oxygen atoms and donor behavior of undercoordinated silver centers (-0.1e).

Furthermore, the electronic structure of $AgNbO_3$ surfaces was analyzed after the H_2O adsorption through the atom-resolved DOS exhibited in **Figure 9**. In all cases, the band gap was slightly reduced compared to pristine surfaces in the adsorption process (Fig. 4). The major changes were observed for (114) surfaces with a reduction of 0.2 eV after the water adsorption. In all cases, it was noted that the highest occupied molecular orbital (HOMO) from water interacts with the Ag/O atomic states. In contrast, the lowest unoccupied molecular orbital (LUMO) interacts with the Nb/O atomic states.

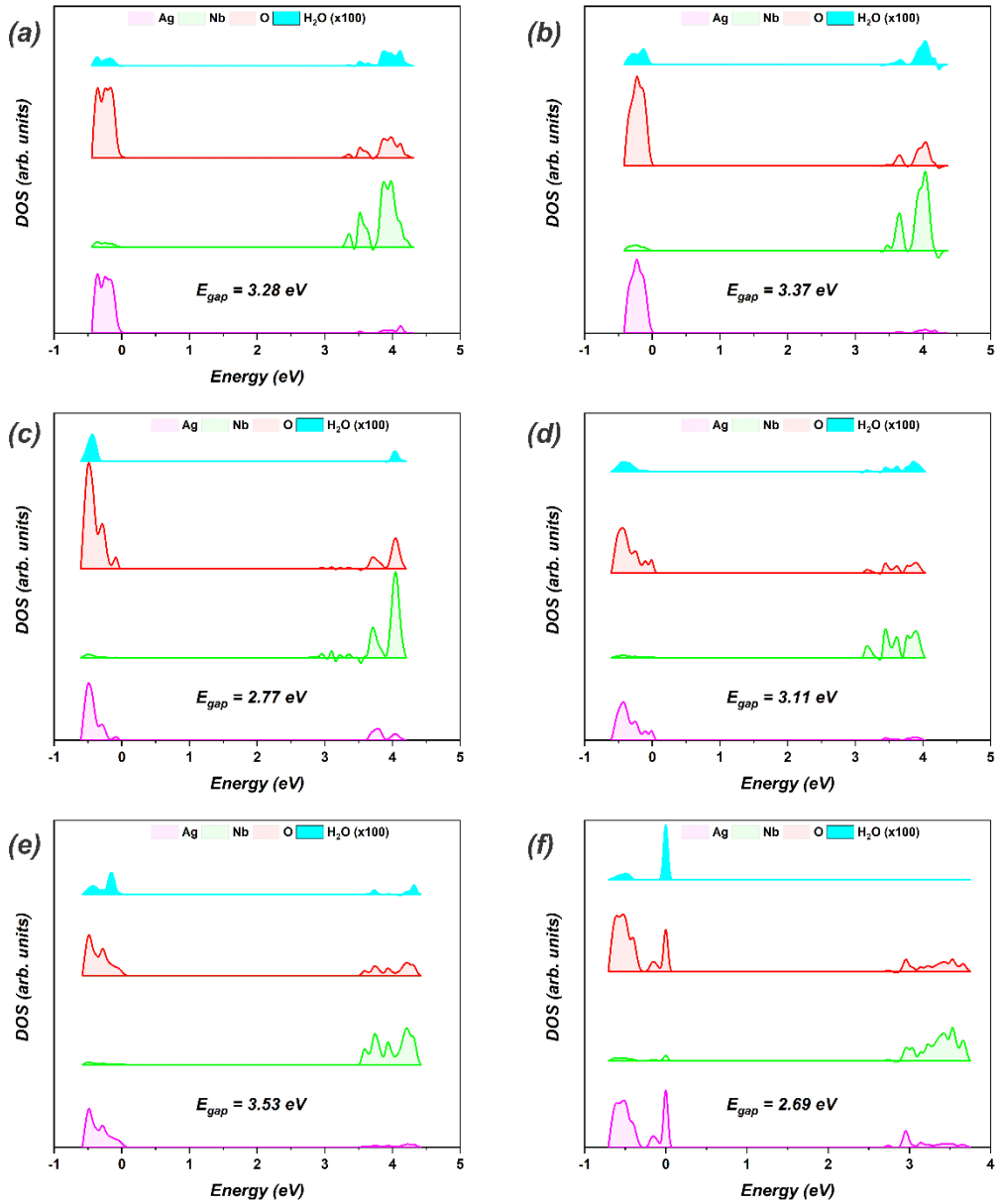

Figure 9. Atom-resolved DOS projections for a) (010), b) (100), c) (110), d) (101), e) (114), and f) (011) surfaces of $AgNbO_3$ after the H_2O adsorption. In all cases, the Fermi level was set at zero.

In the next step, the O_2 adsorption mechanism was evaluated, as exhibited in **Figure 10**.

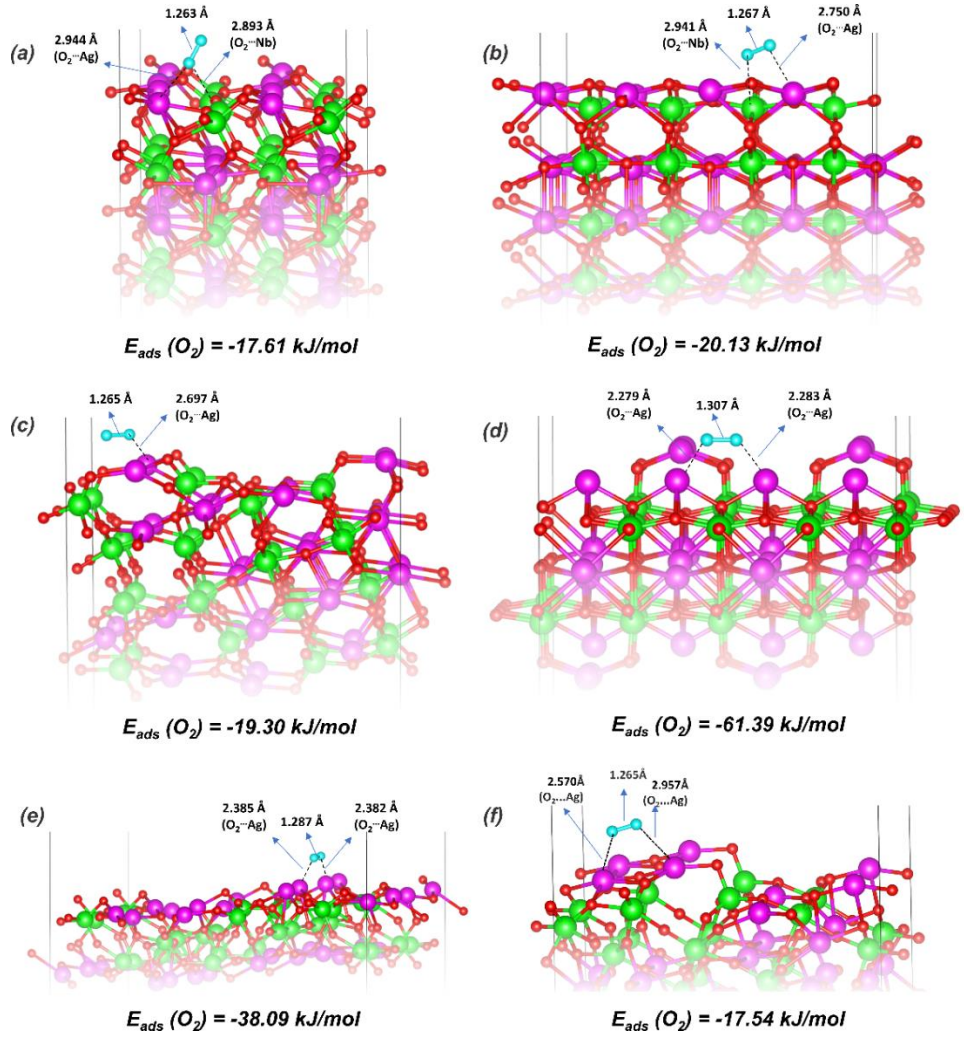

Figure 10. Side views of O_2 adsorption (cyan) on a) (010), b) (100), c) (101), d) (110), e) (114) and f) (011) $AgNbO_3$ surface models. Selected values of Nb-O, Ag-O and O-O distances (Å). Values of the adsorption energies (E_{ads}) were included for comparison purposes.

In this case, it was observed that the O_2 adsorption energies were smaller than for H_2O, and the computed order was (110) > (114) > (100) > (101) > (010) > (011), being the (110) the most active surface. The optimized geometries for O_2 adsorption indicate that bidentate interaction induced the highest adsorption enthalpies for (110) and (114) surfaces. Indeed, for such surfaces the O_2 molecules interact with two superficial Ag-centers, being the major differences associated with the lowest interaction distance for (110) surface, resulting in a most stable interaction. On the other surfaces, the adsorption

mechanism involves only one Ag/Nb center. Furthermore, in all cases the adsorption mechanism can be associated with the physisorption process once no chemical bond was created after the adsorption.

The optimized geometries for (010), (100), and (101) surfaces (**Figures 10a-c**) indicate that O_2 molecules remain stable after the adsorption process. On the other hand, the O_2 molecules adsorbed on the (110) and (114) (**Figures. 10d-e**) surfaces exhibit an enlarged O-O bond distance, which can be associated with the charge-transfer mechanism that generates the superoxide anion radical $^{\bullet}O_2^-$. In particular, the (114) surface exhibited an O-O bond distance of 1.307 Å, closer to the 1.312 – 1.332 Å values reported in the literature for $^{\bullet}O_2^-$ species.[67]

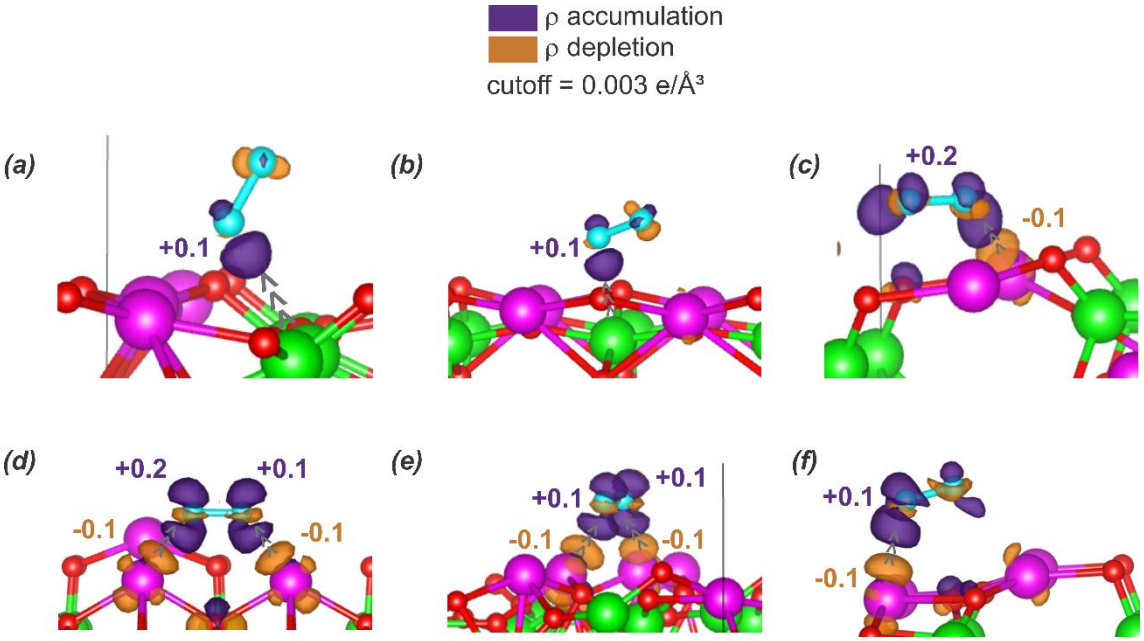

Figure 11. Charge-transfer isosurfaces (0.003 e/Å³) for O_2 (in cyan) adsorption process on a) (010), b) (100), c) (101), d) (110), e) (114) and f) (011) $AgNbO_3$ surface models.

These results were confirmed by the charge-transfer isosurfaces plotted in **Figure 11**. Indeed, the (110) and (114) surfaces exhibit a higher charge-transfer region associated with the bidentate interaction of O_2 molecules with the superficial undercoordinated Ag centers (**Figure 11d-e**). In this case, the undercoordinated Ag donates electrons (-0.1e) to interact with the oxygen atoms that received the electron density (+0.1 or +0.2e). In the opposite direction, the other surfaces exhibited a more reduced charge-transfer region once one interaction path was formed, i. e., only one undercoordinated Ag or Nb center donated electron density (-0.1e) to interact with the O_2 molecules.

In this case, we can argue that the (110) surface is very active for both the H_2O and O_2 adsorption processes. Therefore, as a next step, the coadsorption mechanism was investigated for different types of scenarios ((110) and (114) surfaces) for the coadsorption of O_2 and H_2O on $AgNbO_3$. In (110) surface, the obtained geometry is quite like the individual adsorption exhibited in **Figures 7d** and **10d**, being the coadsorption energy (E_{coads} = -173.08 kJ/mol) almost the sum of the individual values (-173.60 kJ/mol). In the case of (114) surface, unfavorable coadsorption energy (E_{ads} = -89.67 kJ/mol) is observed compared to the sum of the individual values (-103 kJ/mol). Although both surfaces present surface clusters with different vacancies (surface coordination, **see Table 1**) that favor adsorption, the coadsorption process was not favored, which is justified by the arrangement and the poor interaction between O_2 and H_2O molecules on these surfaces; however, despite of our computational efforts in testing different configurations, the best configuration was the one presented.

The electronic structure of O_2-adsorbed surfaces was investigated through the atom-resolved DOS plotted in **Figure 12**. In this case, the band gap was reduced for all surfaces due to the creation of intermediary energy levels within the fundamental band gap region of pristine $AgNbO_3$ surfaces (see **Fig. 4**). These states were associated with the triplet spin-density distributed on antibonding (π^*_{2p}) O_2 orbital, which was located between 0.94 – 1.95 eV.

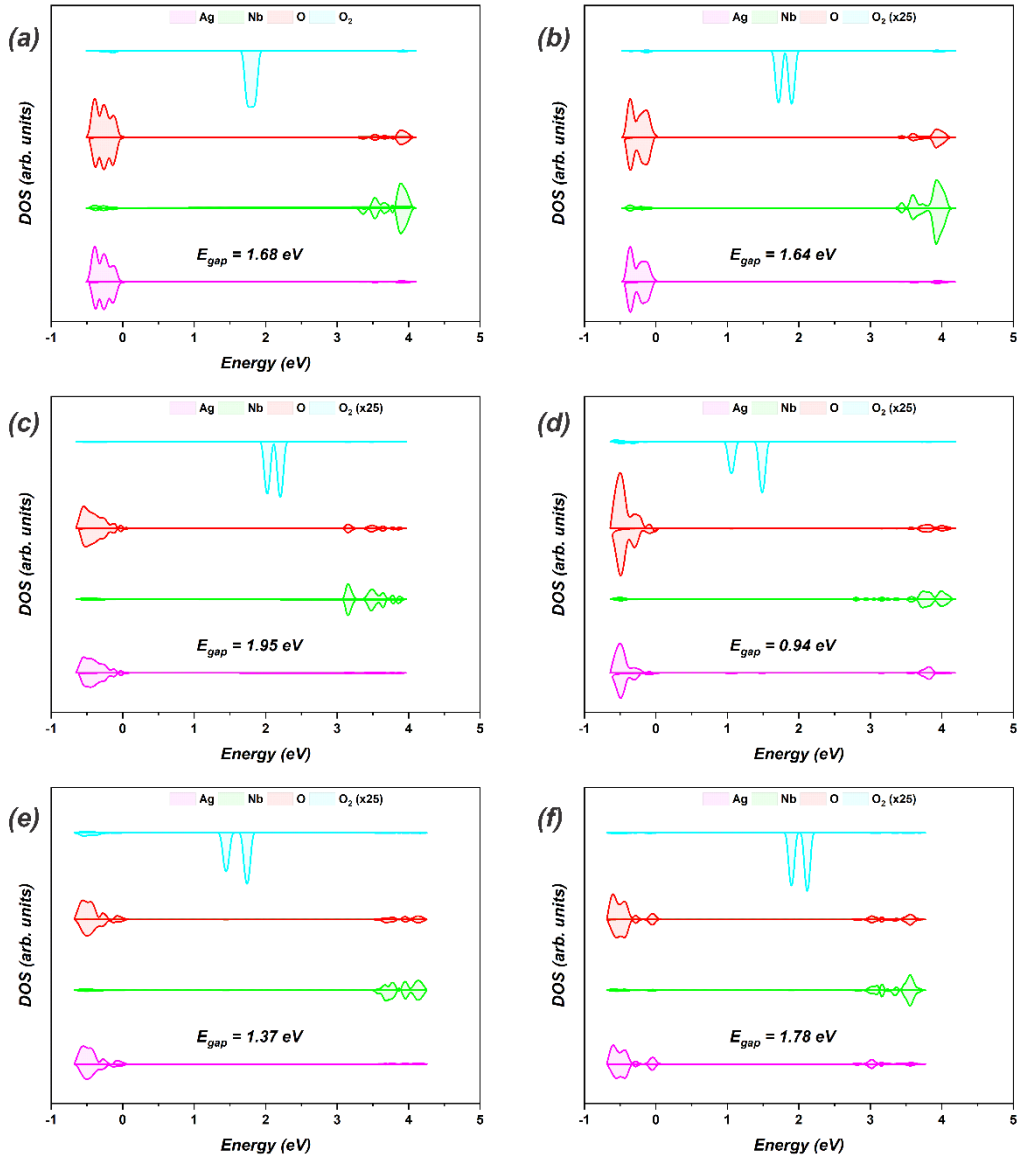

Figure 12. Atom-resolved DOS projections for a) (010), b) (100), c) (110), d) (101), e) (114), and f) (011) surfaces of $AgNbO_3$ after the O_2 adsorption. In all cases, the Fermi level was set at zero.

Subsequently, the coadsorption process was studied on the (010) surface, in which the adsorbed H2O molecules interact with the superficial Nb centers, showing quite favorable adsorption energy. **Figure 13** displays the coadsorption process in the (010) surface, yielding a coadsorption energy (E_{ads} = -115.57 kJ/mol) more stable than the sum of the individual values (-112.74 kJ/mol). Indeed, the computed bond lengths and interaction pathways were calculated and are quite like the individual adsorption (**Figures 7a** and **10a**). The increased stability of the coadsorption structure can be associated with

the smaller changes in the interaction process of the H_2O molecule, while the O_2 showed a more perpendicular adsorption process.

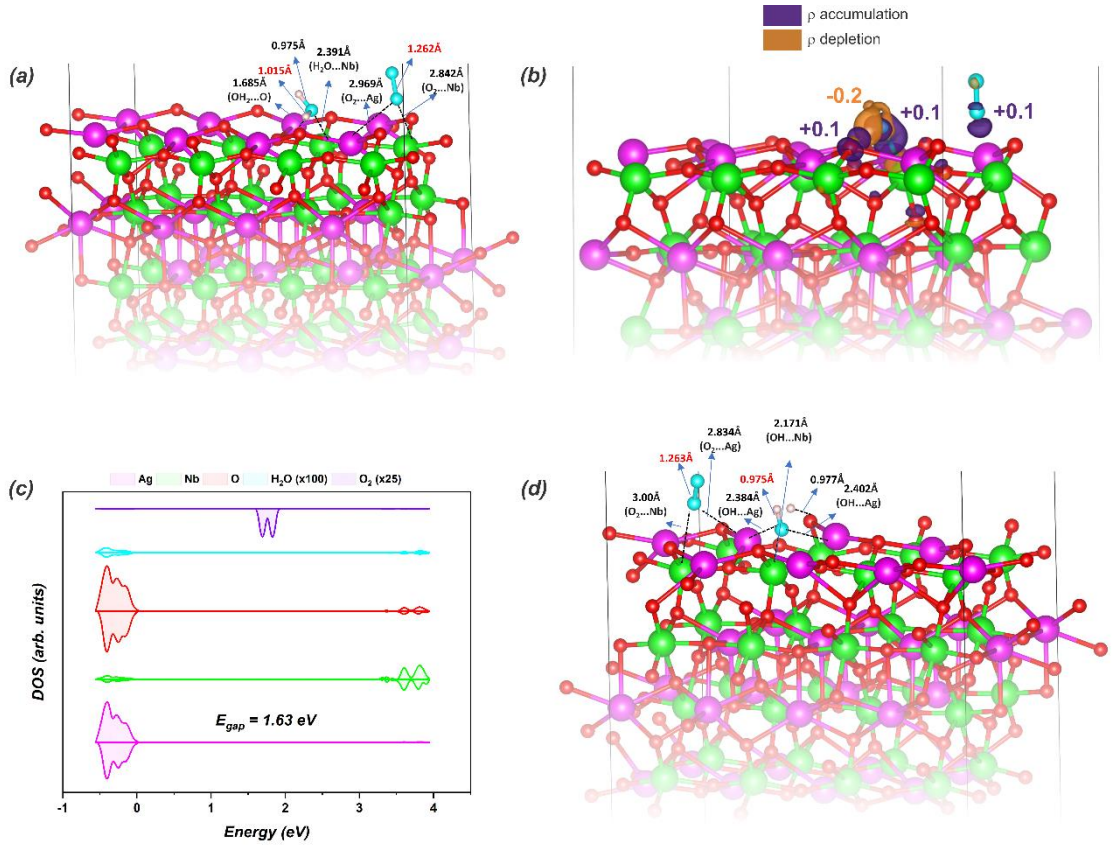

Figure 13. a) Side-view of H_2O/O_2 co-adsorption (cyan) on (010) $AgNbO_3$ surface, b) charge-transfer isosurface (0.003 e/Å^3) and c) atom-resolved DOS. d) Optimized geometry after the H_2O dissociation. Selected values of Nb-O, Ag-O, O-H, and O-O distances (Å).

The electronic structure of the coadsorbed model (**Fig. 13c**) indicates a reduced band gap in comparison to pristine (010) (**Fig. 4a**) mainly due to the triplet spin density localization on antibonding (π^*_{2p}) O_2 orbital, which was located between 1.63 – 2.0 eV. The H_2O atomic states indicate the interaction of HOMO/LUMO orbitals with the fundamental VB and CB of $AgNbO_3$ (010) Surface.

In this case, the coadsorption process modulates an effective charge transfer path from H_2O to O_2, associated with the dissociation mechanism of water molecules to generate hydroxyl radicals •OH and activation of O_2 to form a precursor of superoxide anion radical $^{\bullet}O_2^-$. Indeed, the H_2O acts as an electron donor, yielding a mean Bader charge of 0.10e to the surface of the O anion (2x), resulting in the elongation of the O−H molecular bond from 0.97 to 1.02Å. On the other hand, O_2 simultaneously acts as an

acceptor, capturing a Bader charge of 0.1e from the surface, increasing the O-O bond distance to 1.262 Å, closer to the values reported in the literature for $^{\bullet}O_2^-$ species.[67]

The water dissociation energy was calculated as E_{diss} = -100.28 kJ/mol for the (010) surface with the coadsorbed H_2O/O_2 species. For comparison, the E_{diss} was calculated for the isolated H_2O adsorption, where the computed value was higher (-76.45 kJ/mol) than for the coadsorbed model.

The dissociated •H and •OH adsorb selectively to specific surface sites, i.e., the undercoordinated O anions and Ag/Nb cationic centers, respectively. A twofold coordinated O anion adsorbed with an •H forms an sp^3 electronic configuration with five valence electrons, as shown in **Figure 14(a).** This site is positively charged after releasing one excess electron. The O atom of the •OH adsorbed on the Ag/Nb cation forms, on the other hand, an sp2 electronic configuration with seven electrons, as shown in **Figure 14(b).** This site is negatively charged after it leaves a hole. The twofold coordinated O anion and Ag/Nb catión at the surfaces can be considered as frustrated Lewis base and acid pairs, respectively. These Lewis base and acid sites are electron-rich and electron-deficient with different electronic properties at the surfaces, where the activation of both H_2O and O_2 take place to initiate the formation of adsorbed •OH, •H, and $\bullet O_2^-$ radicals, respectively.

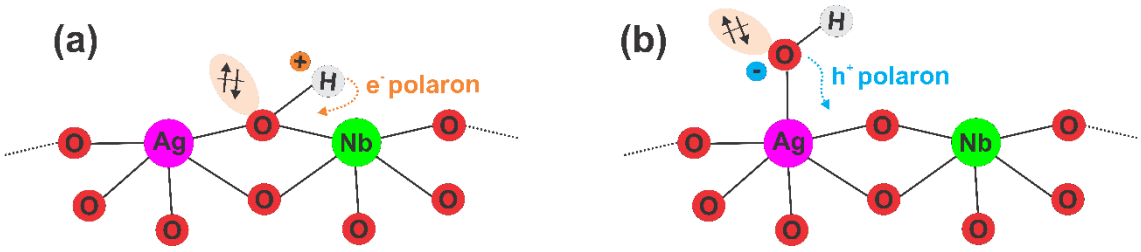

Figure 14. Schematic representation of electronic structures for (a) H-adsorbed and (b) OH-adsorbed on $AgNbO_3$ surfaces after the water dissociation. Excess electrons and holes are donated to the semiconductor surface.

After H_2O dissociates, the excess electrons and holes recombine, while the positively charged •H and the negatively charged •OH remain at the surfaces. The positive and negative charges have been compensated by uniform negative or positive background charges to avoid divergence for the separate calculations of the •H and •OH adsorbed surface structures.[68]

Therefore, the H_2O/O_2 coadsorption process induces a more stable product for the water bond-breaking mechanism, being an important step in ROS generation. When the 4d orbitals of Ag/Nb are coupled to the 2p orbitals of the H_2O and O_2 adsorbates, the Ag/Nb state splits into localized bonding and antibonding states, showing significant overlaps with the 2p orbitals of the O atom, indicating that new bonds were formed and that Ag/Nb atoms can be used as the active site of the homolytic dissociation reaction. In addition, we can also observe that the density of electronic states crosses the Fermi level for the Ag/Nb 4d and O 2p orbitals, introducing abundant unoccupied states near the Fermi energy, which can provide channels for oxygen and hydrogen evolution reactions (OER and HER) associated with the water splitting mechanism.

The optimized model after the dissociation (**Figure 14c**) indicates that the •OH species was stabilized through a stronger interaction with vicinal Ag and Nb centers, while the remaining adsorbed •H interacts with undercoordinated superficial oxygen to generate an OH species linked with Ag/Nb centers. The bond-breaking process approximates the adsorbed O_2 to the Ag center involved in the •OH stabilization. This fact suggests that, after the •OH desorption, the following step involves the •H abstraction from $•O_2^-$ to generate hydroperoxyl radical ($•O_2H$).

4. Conclusions

Ringe et al. write: "Unlike in the bulk, at the nanoscale shape dictates properties" [62]. Thus, investigating the surface of semiconductors based on transition metal oxides is necessary to fully understand and improve their performance and application. In this work, we systematically investigated the stability, structural, and electronic properties of low-index (010), (100), (101), (110), and (011) surfaces, and (114) surface of $AgNbO_3$ using DFT first-principles calculations. Specifically, the active sites at the surfaces, surface energy, the electronic band structure, charge transfer and separation, are analyzed in detail. By analyzing the complexities of interactions of H_2O and O_2 molecules with these surfaces, we shed light on new possibilities for the initial stages of the generation of ROS. Overall, this work offers insights into the surface chemistry and forms the basis for further investigations of catalytic reactions on $AgNbO_3$ surfaces. The main conclusions can be summarized as follows: (i) We have found the following stability order for the studied surfaces: (114) < (100) < (010) < (101) < (011) < (110); (ii) the combination of the calculated values of E_{surf} and Wulff construction was used to forecast the equilibrium morphology (octahedron) and the available morphologies of this material

and their transformations; (iii) the modulation of E_{surf} values has allowed us to obtain the dodecahedron and prismatic morphologies, which match the previously reported FE-SEM and SEM images; (iv) the analysis of CB potentials for bulk and the studied surfaces indicated that excited electrons can activate the adsorbed O_2 molecules to generate the $\cdot O_2^-$ radical. Meanwhile, only (010), (100), and (101) surfaces exhibited VB edges closer to the H_2O/•OH standard potential, making them more reactive for the generation of ·OH radical; (v) the studied surfaces are composed by undercoordinated O anions and Ag and Nb cations, as frustrated Lewis base and acid pairs, respectively. The structure and electronic properties of these active centers control their reactivity; (vi) the values of E_{ads} for H_2O follow this order: (110) > (010) > (101) > (100) > (114) > (011), while for O_2, the order of the E_{ads} values is as follows : (110) > (114) > (100) > (101) > (010) > (011). The E_{ads} of H_2O on the $AgNbO_3$ is superior to that of O_2; (viii) the (110) surface exhibits the strongest E_{ads} for both H_2O and O_2 molecules; (vii) both (110) and (114) surfaces exhibit a higher charge transfer region associated with the double interaction of O_2 molecules with the superficial undercoordinated Ag centers; (viii) the undercoordinated O anions and Ag and Nb cations at the (110) and (010) surfaces selectively bind H_2O and O_2 molecules, opening an exothermically favorable pathway for the initial stages of the formation of reactive oxygen species, ·OH and $\cdot O_2^-$ radicals. Dissociatively adsorbed H_2O yields the precursor of ·H and ·OH radicals, which are adsorbed strongly on both surfaces; (ix) the coadsorption process on the (010) surface induces an effective charge transfer path from H_2O to O_2, to enhance the dissociation of H_2O to generate the precursor of •OH and •H, as well as the activation of O_2 to form the precursor of $^{\bullet}O_2^-$; (x) such charge transfer induced a more favorable dissociation of H_2O for coadsorption process compared to single H_2O adsorption, in the viewpoint of thermodynamics; (xi) present findings reveal a previously unreported chemical mechanism for the generation of these highly reactive species at the surfaces, (xii) our calculations present a solid theoretical analysis of the surface properties of $AgNbO_3$-based materials, providing the theoretical basis for further studies on the catalytic behavior of these exciting materials; (xii) we remark the necessity to describe crucial surface aspects in detail to control the exposure of specific crystal surfaces at the morphology that might be beneficial for the performance of these materials in a wide range of applications, but are challenging to observe with experiments.

Acknowledgments

E. L. and M. C. O. would like to thank the CNPQ, CAPES, and FAPESP (2013/07296-2, 2021/01651-1, and 2022/16840-7) for the financial support. R. A. P. R. acknowledges the FAPEMIG (APQ-00079-21 and APQ-02786-22) and UEMG for the Productivity Program. L. G and J. A. would like to thank Ministerio de Ciencia, Innovación y Universidades (project PID2022-141089NB-I00) and Conselleria d'innovació, Universitats, Ciencia i Societat Digital (CIAICO/2021/122). S.C.S.L has been funded by the postdoctoral program of Jaume I University (POSDOC/2021/18). The authors are also grateful to the National Laboratory for Scientific Computing (LNCC), the High-Performance Computing Center (NACAD) at COPPE-UFRJ, and the National Center for High-Performance Computing (CENAPAD) at UNICAMP for providing computing resources.

References

1. Bai, S., et al., *Facet-Engineered Surface and Interface Design of Photocatalytic Materials.* Advanced Science, 2017. **4**(1): p. 1600216.
2. Gao, L., et al., *Recent advances in activating surface reconstruction for the high-efficiency oxygen evolution reaction.* Chemical Society Reviews, 2021. **50**(15): p. 8428-8469.
3. Raizada, P., et al., *Surface defect engineering of metal oxides photocatalyst for energy application and water treatment.* Journal of Materiomics, 2021. **7**(2): p. 388-418.
4. Hwang, J., et al., *Perovskites in catalysis and electrocatalysis.* Science, 2017. **358**(6364): p. 751-756.
5. Tu, W., et al., *State-of-the-art advancements of crystal facet-exposed photocatalysts beyond TiO2: Design and dependent performance for solar energy conversion and environment applications.* Materials Today, 2020. **33**: p. 75-86.
6. Zaera, F., *Designing Sites in Heterogeneous Catalysis: Are We Reaching Selectivities Competitive With Those of Homogeneous Catalysts?* Chemical Reviews, 2022. **122**(9): p. 8594-8757.
7. Bai, S., et al., *Steering charge kinetics in photocatalysis: intersection of materials syntheses, characterization techniques and theoretical simulations.* Chemical Society Reviews, 2015. **44**(10): p. 2893-2939.
8. Zhang, C., et al., *Surface modeling of photocatalytic materials for water splitting.* Physical Chemistry Chemical Physics, 2022. **24**(3): p. 1237-1261.
9. Inoue, T., et al., *Photoelectrocatalytic reduction of carbon dioxide in aqueous suspensions of semiconductor powders.* Nature, 1979. **277**(5698): p. 637-638.
10. Suzuki, T., et al., *Tuning of photocatalytic reduction by conduction band engineering of semiconductor quantum dots with experimental evaluation of the band edge potential.* Chemical Communications, 2016. **52**(36): p. 6185-6188.
11. Blaser, H., et al., *TNF and ROS Crosstalk in Inflammation.* Trends in Cell Biology, 2016. **26**(4): p. 249-261.
12. Egea, G., F. Jiménez-Altayó, and V. Campuzano, *Reactive Oxygen Species and Oxidative Stress in the Pathogenesis and Progression of Genetic Diseases of the Connective Tissue.* Antioxidants, 2020. **9**(10): p. 1013.
13. Chio, I.I.C. and D.A. Tuveson, *ROS in Cancer: The Burning Question.* Trends in Molecular Medicine, 2017. **23**(5): p. 411-429.

14. Zhang, C., et al., *Progress and challenges in photocatalytic disinfection of waterborne Viruses: A review to fill current knowledge gaps.* Chemical Engineering Journal, 2019. **355**: p. 399-415.
15. Habibi-Yangjeh, A., et al., *Review on heterogeneous photocatalytic disinfection of waterborne, airborne, and foodborne viruses: Can we win against pathogenic viruses?* Journal of Colloid and Interface Science, 2020. **580**: p. 503-514.
16. Pandey, S., et al., *Recent Advancement in Visible-Light-Responsive Photocatalysts in Heterogeneous Photocatalytic Water Treatment Technology*, in *Photocatalysts in Advanced Oxidation Processes for Wastewater Treatment*. 2020. p. 167-196.
17. Sengupta, D., S. Naskar, and D. Mandal, *Reactive oxygen species for therapeutic application: Role of piezoelectric materials.* Physical Chemistry Chemical Physics, 2023. **25**(38): p. 25925-25941.
18. Kubota, K., et al., *Redox reactions of small organic molecules using ball milling and piezoelectric materials.* Science, 2019. **366**(6472): p. 1500-1504.
19. Wu, H., et al., *Recent advances of semiconductor photocatalysis for water pollutant treatment: mechanisms, materials and applications.* Physical Chemistry Chemical Physics, 2023. **25**(38): p. 25899-25924.
20. Caselli, L., et al., *Boosting Membrane Interactions and Antimicrobial Effects of Photocatalytic Titanium Dioxide Nanoparticles by Peptide Coating.* Small. **n/a**(n/a): p. 2309496.
21. Mamaghani, A.H., F. Haghighat, and C.-S. Lee, *Photocatalytic oxidation technology for indoor environment air purification: The state-of-the-art.* Applied Catalysis B: Environmental, 2017. **203**: p. 247-269.
22. Tian, Y., et al., *Silver niobate perovskites: structure, properties and multifunctional applications.* Journal of Materials Chemistry A, 2022. **10**(28): p. 14747-14787.
23. Shan, K., et al., *Ti-Doped AgNbO3 as Novel Dense Diffusion Barriers of Limiting Current Oxygen Sensors.* Langmuir, 2024. **40**(7): p. 3659-3666.
24. Wang, Z., et al., *Effect of AgNbO3 Morphology on Dielectric and Energy Storage Properties of Polyvinylidene Fluoride-Based Nanocomposites.* ACS Applied Nano Materials, 2023. **6**(15): p. 14374-14382.
25. Zhang, Y., et al., *Direct photoluminescence manipulation in Er-doped AgNbO3 lead-free antiferroelectrics via reversible electric-field-induced symmetry modulations.* Ceramics International, 2023. **49**(18): p. 30409-30416.
26. An, K., et al., *Enhanced Energy Storage Performance of AgNbO3:xCeO2 by Synergistic Strategies of Tolerance Factor and Density Regulations.* Coatings, 2023. **13**(3): p. 534.
27. Huang, J., et al., *Greatly enhanced energy storage and discharge properties of AgNbO3 ceramics with a stable antiferroelectric phase and high breakdown strength using hydrothermally synthesized powders.* Journal of Materials Chemistry A, 2022. **10**(30): p. 16337-16350.
28. Shu, L., et al., *Phase-pure antiferroelectric AgNbO3 films on Si substrates: chemical solution deposition and phase transitions.* Journal of Materials Chemistry A, 2022. **10**(23): p. 12632-12642.
29. Talebpour, C., et al., *Nondegradable Antimicrobial Silver-Based Perovskite.* ACS Sustainable Chemistry & Engineering, 2022. **10**(15): p. 4922-4928.
30. Lu, Z., et al., *Mechanism of enhanced energy storage density in AgNbO3-based lead-free antiferroelectrics.* Nano Energy, 2021. **79**: p. 105423.
31. Luo, N., et al., *Constructing phase boundary in AgNbO3 antiferroelectrics: pathway simultaneously achieving high energy density and efficiency.* Nature Communications, 2020. **11**(1): p. 4824.
32. Zhu, L.-F., et al., *Composition and strain engineered AgNbO3-based multilayer capacitors for ultra-high energy storage capacity.* Journal of Materials Chemistry A, 2021. **9**(15): p. 9655-9664.

33. Yang, X., et al., *Enhanced Piezo-photocatalytic Performances of AgNbO3 Materials for Dye Decomposition Via Polarization Engineering.* ChemPhotoChem, 2024. **8**(2): p. e202300142.
34. Khor, C.M., M.M. Khan, and M.H. Harunsani, *Silver niobate-based photocatalysts: Relevance in dye degradation.* Chemical Physics Impact, 2023. **6**: p. 100141.
35. Jiang, L., et al., *High photocatalytic performance of ferroelectric AgNbO3 in a doping state.* Journal of Environmental Chemical Engineering, 2023. **11**(5): p. 110402.
36. Lipsky, F., et al., *A Tale of Reactive Oxygen Species on the Ag3PO4(110) Surface.* The Journal of Physical Chemistry C, 2023. **127**(48): p. 23235-23245.
37. Demichelis, R., et al., *On the performance of eleven DFT functionals in the description of the vibrational properties of aluminosilicates.* International Journal of Quantum Chemistry, 2010. **110**(2): p. 406-415.
38. Dovesi, R., et al., *Quantum-Mechanical Condensed Matter Simulations with CRYSTAL.* Wiley Interdiscip. Rev.: Comput. Mol. Sci., 2018. **8**(4): p. e1360.
39. Joshi, P.K., et al., *Validation of hybrid WC1LYP functional for ferroelectric LiNbO3 and LiTaO3 using Compton spectroscopy and first-principles computations.* Materials Today Communications, 2022. **31**: p. 103288.
40. Aprà, E., et al., *An Ab Initio Hartree-Fock Study of Silver Chloride.* Chemical Physics Letters, 1991. **186**(4): p. 329-335.
41. Sophia, G., et al., *First-principles study of the mechanisms of the pressure-induced dielectric anomalies in ferroelectric perovskites.* Phase Transitions, 2013. **86**(11): p. 1069-1084.
42. Vilela Oliveira, D., et al., *BSSE-correction scheme for consistent gaussian basis sets of double- and triple-zeta valence with polarization quality for solid-state calculations.* Journal of Computational Chemistry, 2019. **40**(27): p. 2364-2376.
43. Gao, B., et al., *Enhanced visible-light-driven photocatalytic performance of AgNbO3 cubes with a high-energy (001) facet.* Journal of Physics and Chemistry of Solids, 2019. **135**: p. 109083.
44. Ribeiro, R.A.P., et al., *Connecting the surface structure, morphology and photocatalytic activity of Ag2O: An in depth and unified theoretical investigation.* Applied Surface Science, 2020. **509**: p. 145321.
45. Jagadeesha Angadi, V., et al., *Unveiling the shape-selective $CoCr_{2-y}Sc_yO_4$ nanomagnetism.* Applied Surface Science, 2022. **574**: p. 151555.
46. Gouveia, A.F., et al., *Modulating the properties of multifunctional semiconductors by means of morphology: Theory meets experiments.* Computational Materials Science, 2021. **188**: p. 110217.
47. Gouveia, A.F., et al., *The hinge morphology of SnO2 as multifunctional semiconductor: What we can learn from simulations, theory, and experiments.* Applied Surface Science, 2023. **622**: p. 156904.
48. Henkelman, G., A. Arnaldsson, and H. Jónsson, *A fast and robust algorithm for Bader decomposition of charge density.* Computational Materials Science, 2006. **36**(3): p. 354-360.
49. Sanville, E., et al., *Improved grid-based algorithm for Bader charge allocation.* Journal of Computational Chemistry, 2007. **28**(5): p. 899-908.
50. Tang, W., E. Sanville, and G. Henkelman, *A grid-based Bader analysis algorithm without lattice bias.* Journal of Physics: Condensed Matter, 2009. **21**(8): p. 084204.
51. Yu, M. and D.R. Trinkle, *Accurate and efficient algorithm for Bader charge integration.* The Journal of Chemical Physics, 2011. **134**(6): p. 064111.
52. Carrasco-Jaim, O.A., L.M. Torres-Martínez, and E. Moctezuma, *Enhanced photocatalytic hydrogen production of AgMO3 (M = Ta, Nb, V) perovskite materials using CdS and NiO as co-catalysts.* Journal of Photochemistry and Photobiology A: Chemistry, 2018. **358**: p. 167-176.

53. Ph, S., et al., *Structural investigation of AgNbO3 phases using x-ray and neutron diffraction.* Journal of Physics: Condensed Matter, 2004. **16**(16): p. 2795.
54. Moriwake, H., et al., *8 - First-principles study of the ferroelectric phase of AgNbO3*, in *Nanoscale Ferroelectric-Multiferroic Materials for Energy Harvesting Applications*, H. Kimura, Z. Cheng, and T. Jia, Editors. 2019, Elsevier. p. 137-159.
55. Chao, W., et al., *Achieving excellent energy storage performance with thermal stability in lead-free AgNbO3 ceramics.* Dalton Transactions, 2024. **53**(7): p. 2949-2956.
56. Kröger, F.A. and H.J. Vink, *Relations between the Concentrations of Imperfections in Crystalline Solids*, in *Solid State Physics*, F. Seitz and D. Turnbull, Editors. 1956, Academic Press. p. 307-435.
57. Andrés, J., et al., *Effects of surface stability on the morphological transformation of metals and metal oxides as investigated by first-principles calculations.* Nanotechnology, 2015. **26**(40): p. 405703.
58. Ferrer, M.M., et al., *A 3D platform for the morphology modulation of materials: first principles calculations on the thermodynamic stability and surface structure of metal oxides: Co3O4, α-Fe2O3, and In2O3.* Modelling and Simulation in Materials Science and Engineering, 2016. **24**(2): p. 025007.
59. Arney, D., et al., *Flux synthesis of AgNbO3: Effect of particle surfaces and sizes on photocatalytic activity.* Journal of Photochemistry and Photobiology A: Chemistry, 2010. **214**(1): p. 54-60.
60. Elumalai, N.K., et al., *Metal oxide semiconducting interfacial layers for photovoltaic and photocatalytic applications.* Materials for Renewable and Sustainable Energy, 2015. **4**(3): p. 11.
61. Maeda, K. and K. Domen, *Solid Solution of GaN and ZnO as a Stable Photocatalyst for Overall Water Splitting under Visible Light.* Chemistry of Materials, 2010. **22**(3): p. 612-623.
62. Xu, Y. and M.A.A. Schoonen, *The absolute energy positions of conduction and valence bands of selected semiconducting minerals.* American Mineralogist, 2000. **85**(3-4): p. 543-556.
63. Jiang, D. and W. Wang, *Chapter 11 - Fundamental Studies on Photocatalytic Structures With Well-Defined Crystal Facets*, in *Studies in Surface Science and Catalysis*, P. Fornasiero and M. Cargnello, Editors. 2017, Elsevier. p. 409-438.
64. Wang, S., A. Lu, and C.-J. Zhong, *Hydrogen production from water electrolysis: role of catalysts.* Nano Convergence, 2021. **8**(1): p. 4.
65. Avcıoğlu, C., et al., *Solar hydrogen generation using niobium-based photocatalysts: design strategies, progress, and challenges.* Materials Today Energy, 2022. **24**: p. 100936.
66. Yan, T., et al., *Bismuth atom tailoring of indium oxide surface frustrated Lewis pairs boosts heterogeneous CO2 photocatalytic hydrogenation.* Nature Communications, 2020. **11**(1): p. 6095.
67. Hayyan, M., M.A. Hashim, and I.M. AlNashef, *Superoxide Ion: Generation and Chemical Implications.* Chemical Reviews, 2016. **116**(5): p. 3029-3085.
68. Kato, K., N. Nagatsuka, and K. Fukutani, *H2 Molecule Generation from Dissociatively Adsorbed Water on TiO2 through Photoexcitation.* The Journal of Physical Chemistry C, 2024. **128**(20): p. 8188-8198.